

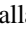
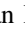










The Atacama Cosmology Telescope: CO($J = 3 - 2$) Mapping and Lens Modeling of an ACT-selected Dusty Star-forming Galaxy

Jesus Rivera¹ , Andrew J. Baker¹ , Patricio A. Gallardo², Megan B. Gralla³, Andrew I. Harris⁴ , Kevin M. Huffenberger⁵ , John P. Hughes¹ , Charles R. Keeton¹ , Carlos H. López-Caraballo⁶, Tobias A. Marriage⁷, Bruce Partridge⁸ , Jonathan L. Sievers^{9,10} , Amitpal S. Tagore¹¹, Fabian Walter¹² , Axel Weiß¹³, and Edward J. Wollack¹⁴ 

¹ Department of Physics and Astronomy, Rutgers, the State University of New Jersey, 136 Frelinghuysen Road, Piscataway, NJ 08854-8019, USA; jrivera@physics.rutgers.edu

² Department of Physics, Cornell University, 109 Clark Hall, Ithaca, NY 14853-2501, USA

³ Steward Observatory, University of Arizona, 933 North Cherry Avenue, Tucson, AZ 85721, USA

⁴ Department of Astronomy, University of Maryland, College Park, MD 20742-2421, USA

⁵ Department of Physics, Florida State University, Tallahassee, FL 32306, USA

⁶ Instituto de Astrofísica and Centro de Astro-Ingeniería, Facultad de Física, Pontificia Universidad Católica de Chile, Av. Vicuña Mackenna 4860, 7820436 Macul, Santiago, Chile

⁷ Department of Physics and Astronomy, The Johns Hopkins University, 3400 North Charles Street, Baltimore, MD 21218-2686, USA

⁸ Department of Physics and Astronomy, Haverford College, Haverford, PA 19041, USA

⁹ University of KwaZulu-Natal, Durban, South Africa National Institute for Theoretical Physics, Durban 4000, KwaZulu-Natal, South Africa

¹⁰ Department of Physics, McGill University, Montreal, QC H3A 2T8, Canada

¹¹ Jodrell Bank Centre for Astrophysics, The University of Manchester, Manchester M13 9PL, UK

¹² Max-Planck-Institut für Astronomie, Königstuhl 17, D-69117, Heidelberg, Germany

¹³ Max-Planck-Institut für Radioastronomie, Auf dem Hügel 69, D-53121 Bonn, Germany

¹⁴ NASA/Goddard Space Flight Center, Greenbelt, MD 20771, USA

Received 2018 July 23; revised 2019 May 28; accepted 2019 May 31; published 2019 July 11

Abstract

We report Northern Extended Millimeter Array CO($J = 3 - 2$) observations of the dusty star-forming galaxy ACT-S J020941+001557 at $z = 2.5528$, which was detected as an unresolved source in the Atacama Cosmology Telescope (ACT) equatorial survey. Our spatially resolved spectral line data support the derivation of a gravitational lens model from 37 independent velocity channel maps using a pixel-based algorithm, from which we infer a velocity-dependent magnification factor $\mu \approx 7-22$ with a luminosity-weighted mean $\langle \mu \rangle \approx 13$. The resulting source-plane reconstruction is consistent with a rotating disk, although other scenarios cannot be ruled out by our data. After correction for lensing, we derive a line luminosity $L'_{\text{CO}(3-2)} = (5.53 \pm 0.69) \times 10^{10} \text{ K km s}^{-1} \text{ pc}^2$, a cold gas mass $M_{\text{gas}} = (3.86 \pm 0.33) \times 10^{10} M_{\odot}$, a dynamical mass $M_{\text{dyn}} \sin^2 i = 3.9^{+1.8}_{-1.5} \times 10^{10} M_{\odot}$, and a gas mass fraction $f_{\text{gas}} \csc^2 i = 1.0^{+0.8}_{-0.4}$. The line brightness temperature ratio of $r_{3,1} \approx 1.6$ relative to a Green Bank Telescope CO($J = 1 - 0$) detection may be elevated by a combination of external heating of molecular clouds, differential lensing, and/or pointing errors.

Key words: galaxies: high-redshift – galaxies: ISM – galaxies: starburst – gravitational lensing: strong

1. Introduction

The characterization of dusty star-forming galaxies (DSFGs) at high redshift entered a new era with the discovery of submillimeter galaxies (Smail et al. 1997; Barger et al. 1998; Hughes et al. 1998). These pioneering studies and their successors revealed a large, previously unknown population of star-forming systems in which dust absorbs nearly all of the UV and optical emission radiated from stars and active galactic nuclei (AGN) and reemits it in the far-infrared/submillimeter regime. DSFGs, now defined more broadly to include systems selected at wavelengths other than the submillimeter, play a critical role in the history of galaxy formation and evolution. They are substantial contributors to the cosmic star formation history and the likely progenitors of nearby elliptical galaxies (Blain et al. 2002; Casey et al. 2014). However, our understanding of these galaxies is still limited by our ability to detect and to study them in detail; recent efforts by many teams have focused on this goal.

Wide-field surveys that map areas greater than 100 deg^2 with sufficient angular resolution have been used to discover gravitationally lensed DSFGs at far-IR and (sub)millimeter wavelengths with *Herschel* (Negrello et al. 2010; Wardlow

et al. 2013; Nayyeri et al. 2016), the South Pole Telescope (Vieira et al. 2010; Mocanu et al. 2013), the Atacama Cosmology Telescope (ACT; Marsden et al. 2014), and *Planck* (Cañameras et al. 2015). High flux density tails on observed number count distributions have proved to be a mixture of strongly lensed DSFGs, clusters of DSFGs, and “trainwreck” systems in which complex mergers of multiple, modestly lensed DSFGs are blended into a single bright source (Riechers et al. 2011; Fu et al. 2013; Ivison et al. 2013; Miller et al. 2018). Strong lensing enables the study of lens-plane mass distributions (including substructure), while allowing the observation of distant, intrinsically faint galaxies in the source plane that would otherwise be too dim to detect. In order to probe the physical properties of lensed DSFGs, we can observe rotational emission lines (most notably of CO) that trace molecular gas and star-forming material.

In this paper, we present CO($J = 3 - 2$) observations of the $z = 2.5528$ DSFG ACT-S J020941+001557 (ACT J0209¹⁵) with the Northern Extended Millimeter Array (NOEMA). Section 2 describes previous and new observations; Section 3 analyzes the spectral line properties, gravitational lensing, and

¹⁵ Su et al. (2017) refer to the source as ACT-S J0210+0016.

source-plane gas morphology of ACT J0209; and Section 4 discusses our conclusions. All calculations assume a flat cosmology with $H_0 = 71 \text{ km s}^{-1} \text{ Mpc}^{-1}$, $\Omega_M = 0.27$, and $\Omega_\Lambda = 0.73$.

2. Observations

2.1. Previous Observations

ACT J0209 was detected with ACT (Fowler et al. 2007; Swetz et al. 2011) in a 470 deg^2 equatorial survey at 148, 218, and 277 GHz (Gralla et al. 2019; Su et al. 2017). DSFG candidates were selected based on their 218 GHz flux densities ($>18 \text{ mJy}$) and consistency of their 148–218 GHz spectral indices with thermal dust emission. The ACT equatorial field was purposely designed to overlap the Sloan Digital Sky Survey (SDSS) Stripe 82 footprint (Abazajian et al. 2009) and 1.4 GHz imaging by the Very Large Array (Becker et al. 1995) to facilitate the identification of optical and radio counterparts. Our initial follow-up of the ACT detection of ACT J0209 ($S_{218} = 69.2 \pm 2.7 \text{ mJy}$) was reported in Su et al. (2017) and included CO($J = 1 - 0$) observations with the Robert C. Byrd Green Bank Telescope (GBT) and subsequent low-resolution CO($J = 3 - 2$) imaging with the Combined Array for Research in Millimeter-wave Astronomy (CARMA). The latter data set confirmed a DSFG redshift $z = 2.5528$ in excess of the SDSS redshift for its optical counterpart ($z_{\text{lens}} = 0.202$), highly suggestive of lensing. The source’s redshift, lensed status, and radio-loud AGN were first reported by Geach et al. (2015), who designated it as 9io9 and dubbed it the “Red Radio Ring” following its identification in a citizen science project to find lenses. Shortly before the submission of this manuscript, Geach et al. (2018) reported an analysis of $\sim 0''.25$ resolution Atacama Large Millimeter/submillimeter Array (ALMA) observations of ACT J0209 in the CO($J = 4 - 3$), CI($J = 1 - 0$), and CN($N = 4 - 3$) lines, which we discuss further below. For our assumed cosmology, $D_A = 679 \text{ Mpc}$ (1.68 Gpc) and $D_L = 982 \text{ Mpc}$ (21.2 Gpc) at $z_{\text{lens}} = 0.202$ ($z = 2.5528$).

2.2. New NOEMA Observations

We observed ACT J0209 with NOEMA on 2016 December 28 and 2017 January 8 (program W16DX; PI: A. Weiß), targeting a J2000 position of $\alpha = 02^{\text{h}} 09^{\text{m}} 40^{\text{s}}.80$ and $\delta = +00^{\text{h}} 15^{\text{m}} 57^{\text{s}}.60$. The array’s eight 15 m diameter antennas were deployed in the A configuration with a longest baseline of 760 m. Receivers were tuned to 97.33 GHz to detect CO($J = 3 - 2$) emission at a redshift $z = 2.5528$. The total on-source integration time after combining both days and flagging bad data was 11.3 hr. We reduced the NOEMA data using the Institut de Radioastronomie Millimétrique (IRAM) GILDAS software (Gildas Team 2013). The sensitivity achieved for robust weighting and deconvolution with the CLEAN algorithm is $0.5 \text{ mJy beam}^{-1}$ in a 20 km s^{-1} channel. We used 3C454.3 as a bandpass calibrator, 0221+067 and 0215+015 as complex gain calibrators, and MWC349 as a flux calibrator, for which we adopted a flux density of 1.14 Jy at 97.3 GHz with $\sim 10\%$ uncertainty (e.g., Trippe et al. 2012).

3. Results

3.1. Integrated Line Properties

We detect and spatially resolve the CO($J = 3 - 2$) emission from ACT J0209; including a 10% uncertainty in the flux scale,

the observed line flux is $F_{\text{CO}(3-2)} = 20.8 \pm 0.5(\pm 2.1) \text{ Jy km s}^{-1}$, with the line extending over a full width at zero intensity (FWZI) of 720 km s^{-1} , from -190 to $+530 \text{ km s}^{-1}$ relative to the rest frame at $z = 2.5528$ (Figure 1). Our total line flux is consistent with the value of $18.2 \pm 2.0 \text{ Jy km s}^{-1}$ measured with CARMA by Su et al. (2017), suggesting that the much fainter ($9.5 \pm 0.6 \text{ Jy km s}^{-1}$) detection reported by Harrington et al. (2016) from Large Millimeter Telescope observations may be unreliable. Figure 1 also shows the CO($J = 1 - 0$) GBT data presented by Su et al. (2017), from which we measure a line flux $F_{\text{CO}(1-0)} = 1.48 \pm 0.09(\pm 0.05) \text{ Jy km s}^{-1}$, including a term for a 3.5% uncertainty in the reference flux density of 3C48 (Perley & Butler 2013). Our NOEMA and GBT data imply a brightness temperature ratio of $r_{3,1} = 1.56 \pm 0.24$ (higher than inferred by Su et al. (2017) on the basis of the lower-S/N CARMA data). The value of $r_{3,1} \approx 1.6$ is significantly higher than seen in previous studies of DSFGs, which yield typical ratios of $r_{3,1} \approx 0.4\text{--}1.1$ (e.g., Ivison et al. 2011; Harris et al. 2012; Sharon et al. 2016), and cannot be explained using single-zone radiative transfer modeling alone. Su et al. (2017) argued that an elevated line ratio could be due to differential lensing. However, this scenario is disfavored by the broad similarity of the velocity profiles for the GBT CO($J = 1 - 0$) and NOEMA CO($J = 3 - 2$) spectra (Figure 1), which was not previously evident due to the limited S/N of the CARMA data. The CO($J = 4 - 3$) velocity profile observed by Geach et al. (2018), which exhibits the same width and $\sim 3:1$ ratio between peak flux densities on the blue and red sides of the line, again offers no evidence of differential lensing of CO lines. Our observed high $r_{3,1}$ ratio could be due in part to imperfect GBT pointing, which would lead to an underestimated CO($J = 1 - 0$) flux while preserving the line profile. Although one recent independent GBT CO($J = 1 - 0$) observation does imply a lower $r_{3,1} \approx 1.4$ (M. S. Yun 2019, private communication), careful reassessment of our GBT data reveals no evidence that either the overall flux scale (set by cross-calibration of the nearby quasar 2017+0144 against 3C48) or the pointing stability during our session can have reduced ACT J0209’s CO($J = 1 - 0$) flux by more than $\sim 10\%$. Fortunately, there remains an appealing astrophysical explanation. Values of $r_{3,1}$ as high as 1.3–1.4 have been observed in the centers of multiple nearby starburst galaxies (Dumke et al. 2001) and may result from the external heating of molecular clouds whose CO emission is optically thick. In this situation—previously invoked by multiple authors to explain observed values $r_{2,1} > 1$ (e.g., Young & Scoville 1984; Braine & Combes 1992; Turner et al. 1993) in external galaxies, and $r_{3,2} > 1$ in the Orion B molecular cloud (Kramer et al. 1996)—excitation temperature gradients can allow a higher- J CO line to reach $\tau \approx 1$ in clouds’ warmer outer layers even as a lower- J CO line reaches $\tau \approx 1$ only in their cooler cores (e.g., Gierens et al. 1992). For Galactic molecular clouds, such temperature gradients established by external UV irradiation may also help explain anomalous combinations of CO and ^{13}CO intensity ratios (Castets et al. 1990; Pineda & Bensch 2007). We note that the $25.6 \text{ Jy km s}^{-1}$ CO($J = 4 - 3$) flux measured for ACT J0209 by Geach et al. (2018) implies a brightness temperature ratio $r_{4,1} \approx 1.1$, much higher than typical values of 0.2–0.3 in other DSFGs (e.g., Hainline et al. 2006; Harrington et al. 2018). This elevated $r_{4,1}$, like our high $r_{3,1}$,

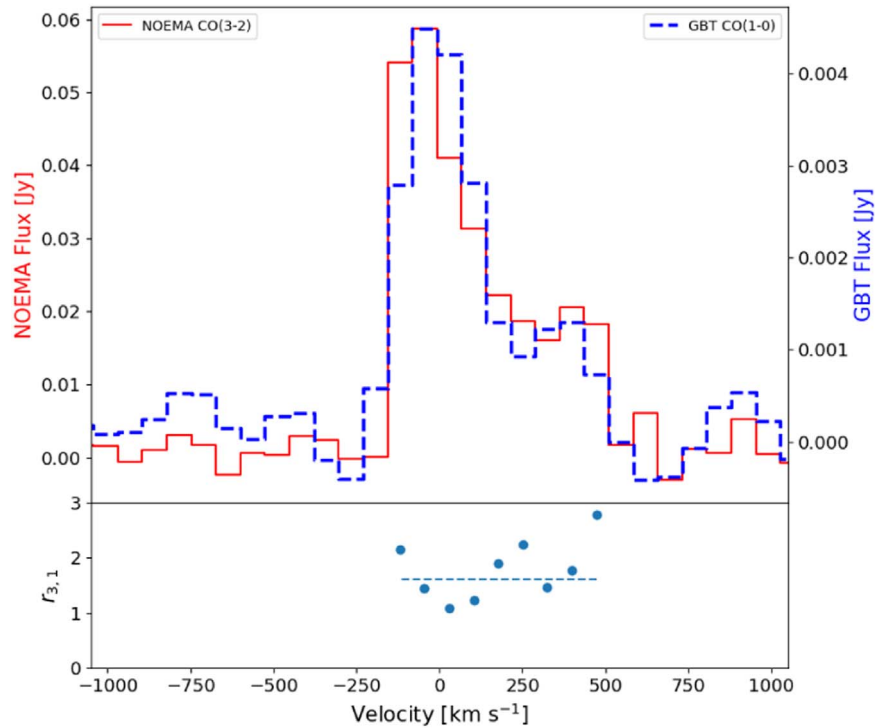


Figure 1. Upper panel: NOEMA CO($J = 3 - 2$) spectrum of ACT J0209 (red) overlaid with the GBT CO($J = 1 - 0$) spectrum (dashed blue). The NOEMA data have been rebinned to match the coarser resolution of the GBT data. Integrated line fluxes are summed over FWZI = 720 km s^{-1} . Lower panel: $r_{3,1}$ ratio on a per-channel basis. The luminosity-weighted global mean ($r_{3,1}$) ≈ 1.6 is indicated as a dashed line.

can be naturally explained by a combination of GBT mispointing and external heating of molecular clouds.

3.2. Lensing Reconstruction and Source-plane CO Properties

Figure 2(a) shows the velocity-integrated line flux (i.e., zeroth-moment) map, which contains an extended arc-like structure and a smaller counterimage. To fit a lens model, we follow Geach et al. (2015) and assume that there are two galaxies in the lens plane: component 1 (C1) represents the brighter galaxy, which we model as a singular isothermal ellipsoid, and component 2 (C2) represents the fainter galaxy, which we model as a singular isothermal sphere. Also including external shear, we vary the 10 lens parameters shown in Table 1. We reconstruct the source using the algorithm described by Tagore & Keeton (2014) and Tagore & Jackson (2016). Briefly, the software treats the source as a collection of shapelets and adjusts them to achieve the best fit to the lensed image subject to a regularization constraint. We checked that the results are robust to different choices of the number of shapelets.

We first fit the lens model to the zeroth-moment map to obtain an initial estimate of parameter values. We then used 37 CO($J = 3 - 2$) channel maps, each 20 km s^{-1} in width, and adjusted the lens model parameters to obtain the best joint fit to all channels. (The sources in the different channels are reconstructed independently.) Our channel-map-based model was informed by *Hubble Space Telescope* (*HST*) F160W imaging of the target (program 14653; PI: J. Lowenthal) in two limited respects. First, we allowed the difference between the positions of the two lensing galaxies to diverge from their difference in the *HST* image by no more than $\pm 0''.1$ in R.A. and decl., and we allowed the absolute positions of both to vary together to accommodate any *HST*/NOEMA astrometric

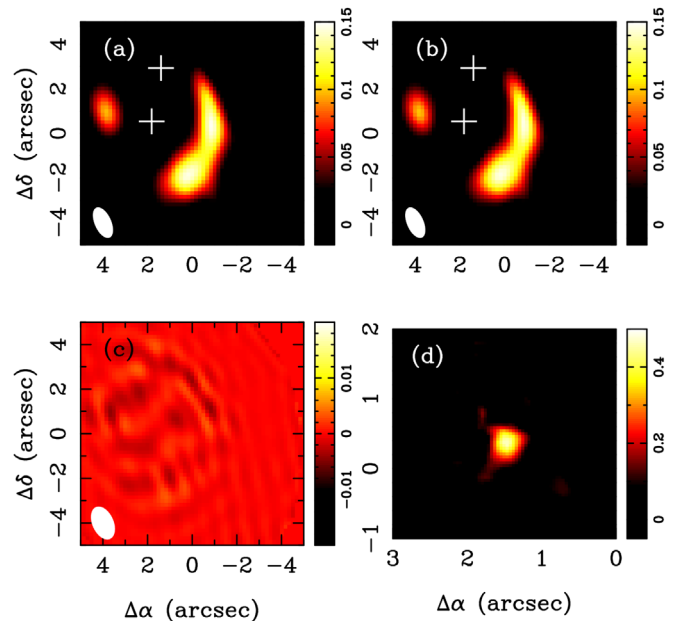


Figure 2. Lens model for ACT J0209 applied to the CO($J = 3 - 2$) moment map. Panel (a) shows the observed moment map; panel (b) shows the model moment map assuming lens parameters from Table 1 and the reconstructed source in panel (d); and panel (c) shows the (data)–(model) residual map. The white crosses in panels (a) and (b) mark the positions of the two lens components. In the image-plane panels, the beam size shown in the lower left corners is $1''.53 \times 0''.74$, and intensity units are $\text{Jy beam}^{-1} \text{ km s}^{-1}$; the source-plane intensity scale differs due to its lower degree of effective smoothing. All panels integrate over $\Delta v = -190 \rightarrow +530 \text{ km s}^{-1}$ relative to systemic redshift.

Table 1
Lens Model Parameters

	b (arcsec)	$\Delta\alpha$ (arcsec)	$\Delta\delta$ (arcsec)	e_c	e_s	γ_c	γ_s
Best							
Component 1	2.444	-0.005	-0.249	-0.206	-0.087
Component 2	0.103	-0.609	2.192
External shear	-0.020	0.015
MCMC median							
Component 1	$2.436^{+0.016}_{-0.010}$	$-0.005^{+0.000}_{-0.001}$	$-0.241^{+0.009}_{-0.007}$	$-0.205^{+0.028}_{-0.019}$	$-0.106^{+0.019}_{-0.015}$
Component 2	$0.107^{+0.007}_{-0.005}$	$-0.570^{+0.048}_{-0.030}$	$2.193^{+0.052}_{-0.030}$
External shear	$-0.0212^{+0.015}_{-0.011}$	$0.0255^{+0.006}_{-0.007}$

Note. The “best” model yielded the single lowest χ^2 model in our MCMC runs and is used for all analyses of reconstructed source-plane emission in this paper. The “MCMC median” model shows the median value of each parameter with uncertainties corresponding to the 16th and 84th percentile ranges derived from the MCMC sampling; the small uncertainties in some positional parameters reflect priors imposed based on *HST* imaging. Due to the complex multidimensional parameter space, not every “best” model parameter falls within the 16th–84th percentile range for the corresponding “MCMC median” distribution. Offsets in R.A. and decl. ($\Delta\alpha$, $\Delta\delta$) are defined relative to the NOEMA pointing center. The singular isothermal ellipsoid has projected surface density $\kappa = b/2\zeta$ as implemented in *gravlens* for coordinate $\zeta \equiv [(1 - \epsilon)x^2 + (1 + \epsilon)y^2]^{1/2}$ with $q^2 \equiv (1 - \epsilon)^2 \equiv (1 - \epsilon)/(1 + \epsilon)$. The ellipsoid’s ellipticity e and the position angle (east of north) of its major axis θ_e are combined into the fit parameters $e_c \equiv e \cos 2\theta_e$ and $e_s \equiv e \sin 2\theta_e$; the external shear γ and its position angle θ_γ are likewise combined into fit parameters γ_c and γ_s .

inconsistency. Second, we used the 3.25 mag difference between the two galaxies’ integrated magnitudes, as measured by GALFIT (Peng et al. 2002) fits to the *HST* image, to estimate a factor of ~ 4.5 difference between the two mass components’ Einstein radii, on the assumption that Einstein radius $b \propto \sigma^2 \propto L^{1/4}$ for an isothermal sphere given the Faber & Jackson (1976) relation. The resulting estimate ($b = 0''.48$) for the companion and the considerably lower value ($b = 0''.16$) preferred by the model of Geach et al. (2015) led us to restrict its Einstein radius to lie in the range $0''.1$ – $0''.5$. While there are some parameter degeneracies, in particular between the mass of the companion and the ellipticity of the main lens, we find that the model converges to lower values of b (and hence mass) regardless of what we adopt as an initial value. After determining our best-fit model parameters (Table 1), we generated reconstructed channel maps (and a reconstructed moment map) for the CO($J = 3 - 2$) data. We then used this best-fit model as the starting point for a Markov Chain Monte Carlo (MCMC) exploration of model parameter space, using the built-in MCMC function found in the *gravlens* software. We started the simulation with 25 walkers and stopped when the solutions for each of the 10 parameters converged. The “MCMC median” portion of Table 1 shows the 16th–84th percentile ranges of the MCMC chains after 500 burn-in steps.

Figure 2 shows the application of our model to the CO($J = 3 - 2$) moment map. Figure 2(b) shows the model of the image plane derived from the lens reconstruction; Figure 2(c) shows a (data)—(model) residual map; and Figure 2(d) shows the source-plane reconstruction. We infer a delensed line flux $F_{\text{CO}(3-2)} = 1.60 \pm 0.20 \text{ Jy km s}^{-1}$ and an intrinsic line luminosity $L'_{\text{CO}(3-2)} = (5.53 \pm 0.69) \times 10^{10} \text{ K km s}^{-1} \text{ pc}^2$. To estimate a cold molecular gas mass, we assume the CO($J = 1 - 0$) and CO($J = 3 - 2$) lines are identically lensed (see above), in which case the intrinsic CO($J = 1 - 0$) luminosity will be $L'_{\text{CO}(1-0)} = (3.55 \pm 0.30) \times 10^{10} \text{ K km s}^{-1} \text{ pc}^2$. Adopting a CO-to-H₂ conversion factor $\alpha_{\text{CO}} = 0.8 M_\odot (\text{K km s}^{-1} \text{ pc}^2)^{-1}$ appropriate for star-forming galaxies and correcting by factor

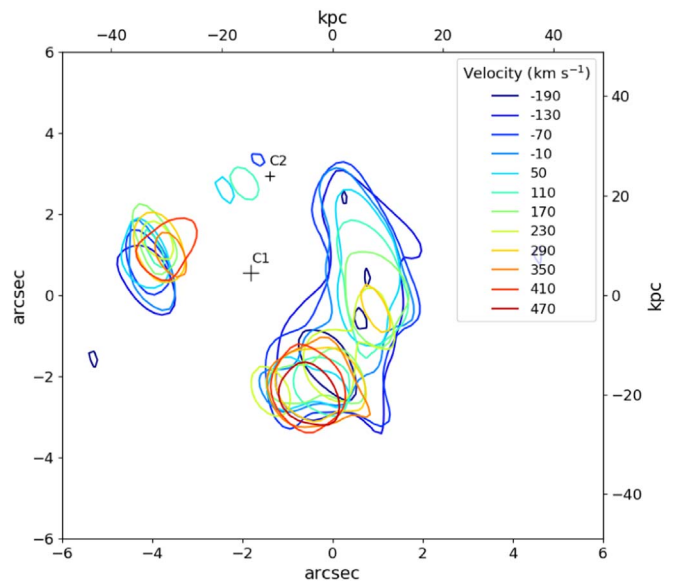


Figure 3. Observed CO($J = 3 - 2$) channel maps of ACT J0209; contours are $4\sigma = 1.92 \text{ mJy beam}^{-1}$. Representative channels shown indicate velocities (in km s^{-1}) relative to $z = 2.5528$. The crosses mark the positions of the two lens components. Axes indicate angular (left, bottom) and projected linear (right, top) scales.

of 1.36 for helium Bolatto et al. (2013), we then infer $M_{\text{gas}} = (3.86 \pm 0.33) \times 10^{10} M_\odot$.

Figures 3 and 4 show channel maps of the raw data and source-plane reconstruction, respectively. The reconstructed channel maps reveal a clear velocity gradient, suggesting that the galaxy is (or at least contains) a rotating disk. Given the very sharp drop-offs on both sides of the velocity profile (see below), we use the second and third most highly redshifted and blueshifted velocity channels to estimate a circular velocity ($v_{\text{circ}} \sin i = 340 \pm 20 \text{ km s}^{-1}$) and a diameter (from emission peaks: $2.9 \pm 0.9 \text{ kpc}$) for the putative disk, and thereby a dynamical mass of $M_{\text{dyn}} \sin^2 i = 3.9^{+1.8}_{-1.5} \times 10^{10} M_\odot$ in terms of an inclination i that we are unable to constrain. The implied

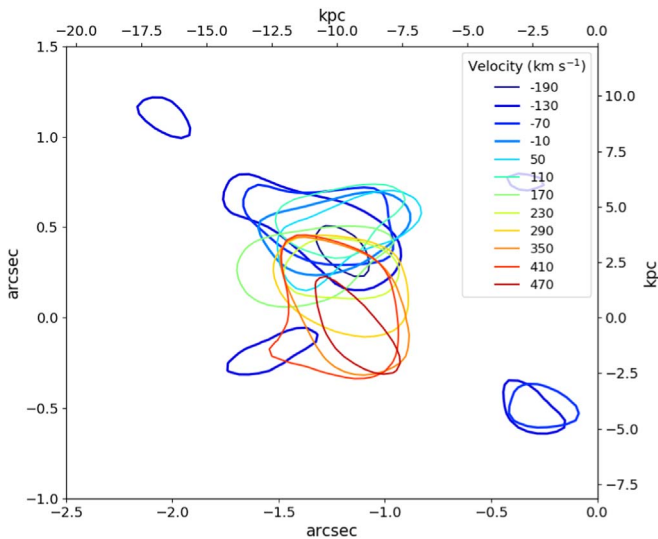


Figure 4. Contours of the source-plane reconstructions for the CO($J = 3 - 2$) channel maps shown in Figure 3. Source-plane reconstructions have spatially varying noise and resolution, so thin (thick) contours are plotted at an approximate 3σ (4σ) level to indicate morphologies. Representative channels shown indicate velocities (in km s^{-1}) relative to $z = 2.5528$. Axes indicate angular (left, bottom) and projected linear (right, top) scales.

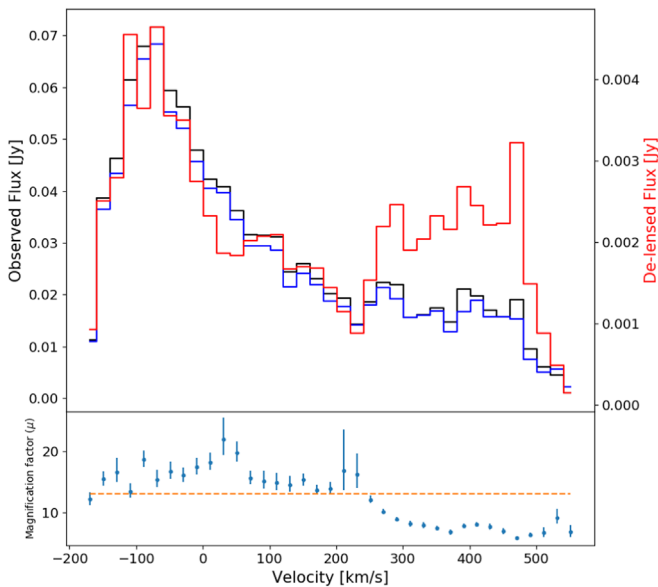


Figure 5. Upper panel: observed CO($J = 3 - 2$) spectrum (black) overlotted with the spectrum of the model channel maps (blue; same scale as observed spectrum, at left) and reconstructed channel maps (red, scale at right). Blue channels (relative to $z = 2.5528$) are more highly magnified than redder channels. Lower panel: ratio between the lensed and delensed spectra, i.e., magnification factor on a per-channel basis, with 16th–84th percentile uncertainties plotted as error bars.

cold gas mass fraction is thus a rather high $f_{\text{gas}} \text{csc}^2 i = 1.0_{-0.4}^{+0.8}$.

The upper panel of Figure 5 shows a spectrum extracted from the reconstructed channel maps (red) and directly compares it to the observed spectrum (black), after scaling the two peaks of the spectra at $\sim -80 \text{ km s}^{-1}$ to match. Also overlotted is a spectrum extracted from the modeled image-plane channel maps (blue), whose good agreement with the observed spectrum validates our lens model. The lower panel shows the inferred magnification factor on a per-channel basis,

calculated by dividing the lensed spectrum by the delensed spectrum. Our lens reconstruction shows that ACT J0209 has a velocity-dependent magnification range of $\mu \approx 7\text{--}22$ with an average of $\mu \approx 13$, which is consistent with the result of Geach et al. (2015) that $\mu_{\text{NIR}} \approx 14$ and $\mu_{5 \text{ GHz}} \approx 13$. We also see that the bluer side of the line (relative to $z = 2.5528$) is more highly magnified than the redder side.

In order to calculate uncertainties in the magnification factors, we use the source brightness covariance matrix associated with our best model to generate 10^4 random sources, lens those sources, and compute the magnification factors for each. The magnification uncertainties shown in the lower panel of Figure 5 correspond to the 16th and 84th percentile ranges of the distributions in μ ; these show channel-to-channel variations that (like the magnifications themselves) depend on S/N and proximity to lensing caustics. We have also assessed the uncertainties in magnification that result from varying the *model* (rather than the source), using the MCMC chains described above. However, we find that model-driven uncertainties are smaller than source-driven uncertainties for all but one of the 37 channels in our data set. Since the two types of uncertainties are not independent and thus cannot be added in quadrature, we opt in Figure 5 to show only the dominant, source-based uncertainties, plotted as 16th–84th percentile error bars.

4. Discussion and Conclusions

We present the first spatially resolved CO($J = 3 - 2$) observations of ACT J0209, obtained with NOEMA, and use the pixel-based source reconstruction technique described in Tagore & Keeton (2014) and Tagore & Jackson (2016) to derive a lens model from the 37 independent velocity channels in our CO data cube. We find that ACT J0209’s CO($J = 3 - 2$) emission is gravitationally magnified by a factor of $\mu \approx 7\text{--}22$ across the galaxy’s velocity profile, with a luminosity-weighted mean $\langle \mu \rangle \approx 13$ consistent with the values found by Geach et al. (2015). The source’s unexpectedly high line brightness temperature ratio of $r_{3,1} \approx 1.6$ is most plausibly due to external heating of molecular clouds, although GBT pointing errors may contribute at a modest level; a differential lensing scenario alone is disfavored since the profiles of the GBT CO($J = 1 - 0$), NOEMA CO($J = 3 - 2$), and ALMA CO($J = 4 - 3$) spectra are broadly similar. To distinguish between these three scenarios, high spectral and spatial resolution CO($J = 1 - 0$) data are needed to identify where the line is emitted within the overall volume relative to CO($J = 3 - 2$).

The delensed properties of ACT J0209 include a CO($J = 3 - 2$) line profile that is still asymmetric across its full FWZI, although less so than the observed spectrum; we conclude that the distribution of molecular gas within the galaxy is not axisymmetric. The velocity gradient seen in the reconstructed source-plane channel maps is, likewise, not symmetric, with blueshifted channels especially tending to lie on top of each other. These asymmetries raise the question of whether we are looking at the superposition of two galaxies (e.g., in an early-stage merger) rather than a single rotating disk. We favor the single-disk interpretation for two reasons: the very sharp drop-offs on both sides of the delensed CO($J = 3 - 2$) spectrum that closely resemble those seen for classical double-horned disk profiles, and excitation as traced by $r_{3,1}$ (and $r_{4,1}$) that does not vary systematically with

velocity, as would be expected for the superposition of two unmerged components (e.g., Sharon et al. 2015). A late-stage merger containing a coalesced molecular disk, on the other hand, remains a possibility.

Geach et al. (2018) have reported an analysis of $\sim 0''.25$ resolution ALMA observations of ACTJ0209 in the CO($J = 4 - 3$), CI($J = 1 - 0$), and CN($N = 4 - 3$) lines. Those authors conclude that the source's CO($J = 4 - 3$) emission arises in a rotating ring whose nearly north/south kinematic major axis, inferred inclination ($i \approx 50^\circ$), and dynamical mass are consistent within uncertainties with our combined constraint on $M_{\text{dyn}} \sin^2 i$. Their best estimate of the cold gas mass from the galaxy's CI($J = 1 - 0$) flux, however, is more than double what is inferred from its CO($J = 1 - 0$) flux in this work. In contrast to our lens model, which is derived from 37 independent CO($J = 3 - 2$) velocity channels, Geach et al. (2018) derive their lens model from an integrated CO($J = 4 - 3$) moment map before applying it to the individual CO($J = 4 - 3$) velocity channels. In this case, the loss of information about the lensing potential that can in principle occur when a spectral line data cube is collapsed into a moment map (see, e.g., Hezaveh et al. 2013) is more than compensated for by the superior resolution and sensitivity of the ALMA data. Our work nevertheless demonstrates the great potential of pixel-based lens modeling for the recovery of nonparametric structures in source-plane channel maps, provided that (as here) observations resolve a source well but do not resolve out significant fractions of its emission.

The authors thank Melanie Krips, Catie Raney, and Anthony Young for helpful interactions, Min Yun for information on unpublished GBT observations, and an anonymous referee for helpful comments. This work was based on observations carried out under project number W16DX with the IRAM NOEMA Interferometer. IRAM is supported by INSU/CNRS (France), MPG (Germany), and IGN (Spain). This work was supported by the U.S. National Science Foundation through awards AST-0955810 to A.J.B., AST-1716585 to C.R.K., and AST-0408698 for the ACT project, along with awards PHY-0855887 and PHY-1214379. Funding was also provided by Princeton University, the University of Pennsylvania, and a Canada Foundation for Innovation (CFI) award to the University of British Columbia. ACT operates in the Parque Astronómico Atacama in northern Chile under the auspices of the Comisión Nacional de Investigación Científica y Tecnológica de Chile (CONICYT). C.L. thanks CONICYT for grant Anillo ACT-1417. Computations were performed on the GPC supercomputer at the SciNet HPC Consortium. SciNet is funded by the CFI under the auspices of Compute Canada, the Government of Ontario, the Ontario Research Fund Research Excellence, and the University of Toronto.

ORCID iDs

Jesus Rivera  <https://orcid.org/0000-0003-3191-5193>

Andrew J. Baker  <https://orcid.org/0000-0002-7892-396X>

Andrew I. Harris  <https://orcid.org/0000-0001-6159-9174>


Kevin M. Huffenberger  <https://orcid.org/0000-0001-7109-0099>

John P. Hughes  <https://orcid.org/0000-0002-8816-6800>

Charles R. Keeton  <https://orcid.org/0000-0001-6812-2467>

Bruce Partridge  <https://orcid.org/0000-0001-6541-9265>

Jonathan L. Sievers  <https://orcid.org/0000-0001-6903-5074>

Fabian Walter  <https://orcid.org/0000-0003-4793-7880>

Edward J. Wollack  <https://orcid.org/0000-0002-7567-4451>

References

- Abazajian, K. N., Adelman-McCarthy, J. K., Agüeros, M. A., et al. 2009, *ApJS*, **182**, 543
- Barger, A. J., Cowie, L. L., Sanders, D. B., et al. 1998, *Natur*, **394**, 248
- Becker, R. H., White, R. L., & Helfand, D. J. 1995, *ApJ*, **450**, 559
- Blain, A. W., Smail, I., Ivison, R. J., Kneib, J.-P., & Frayer, D. T. 2002, *PhR*, **369**, 111
- Bolatto, A. D., Wolfire, M., & Leroy, A. K. 2013, *ARA&A*, **51**, 207
- Braine, J., & Combes, F. 1992, *A&A*, **264**, 433
- Cañameras, R., Nesvadba, N. P. H., Guery, D., et al. 2015, *A&A*, **581**, A105
- Casey, C. M., Narayanan, D., & Cooray, A. 2014, *PhR*, **541**, 45
- Castets, A., Duvert, G., Dutrey, A., et al. 1990, *A&A*, **234**, 469
- Dumke, M., Nieten, C., Thuma, G., Wielebinski, R., & Walsh, W. 2001, *A&A*, **373**, 853
- Faber, S. M., & Jackson, R. E. 1976, *ApJ*, **204**, 668
- Fowler, J. W., Niemack, M. D., Dicker, S. R., et al. 2007, *ApOpt*, **46**, 3444
- Fu, H., Cooray, A., Feruglio, C., et al. 2013, *Natur*, **498**, 338
- Geach, J. E., Ivison, R. J., Dye, S., & Oteo, I. 2018, *ApJL*, **866**, L12
- Geach, J. E., More, A., Verma, A., et al. 2015, *MNRAS*, **452**, 502
- Gierens, K. M., Stutzki, J., & Winnewisser, G. 1992, *A&A*, **259**, 271
- Gildas Team 2013, GILDAS: Grenoble Image and Line Data Analysis Software, Astrophysics Source Code Library, ascl:1305.010
- Gralla, M. B., Marriage, T. A., Addison, G., et al. 2019, *ApJ*, submitted (arXiv:1905.04592)
- Hainline, L. J., Blain, A. W., Greve, T., et al. 2006, *ApJ*, **650**, 614
- Harrington, K. C., Yun, M. S., Cybulski, R., et al. 2016, *MNRAS*, **458**, 4383
- Harrington, K. C., Yun, M. S., Magnelli, B., et al. 2018, *MNRAS*, **474**, 3866
- Harris, A. I., Baker, A. J., Frayer, D. T., et al. 2012, *ApJ*, **752**, 152
- Hezaveh, Y., Dalal, N., Holder, G., et al. 2013, *ApJ*, **767**, 9
- Hughes, D. H., Serjeant, S., Dunlop, J., et al. 1998, *Natur*, **394**, 241
- Ivison, R. J., Papadopoulos, P. P., Smail, I., et al. 2011, *MNRAS*, **412**, 1913
- Ivison, R. J., Swinbank, A. M., Smail, I., et al. 2013, *ApJ*, **772**, 137
- Kramer, C., Stutzki, J., & Winnewisser, G. 1996, *A&A*, **307**, 915
- Marsden, D., Gralla, M., Marriage, T. A., et al. 2014, *MNRAS*, **439**, 1556
- Miller, T. B., Chapman, S. C., Aravena, M., et al. 2018, *Natur*, **556**, 469
- Mocanu, L. M., Crawford, T. M., Vieira, J. D., et al. 2013, *ApJ*, **779**, 61
- Nayyeri, H., Keele, M., Cooray, A., et al. 2016, *ApJ*, **823**, 17
- Negrello, M., Hopwood, R., De Zotti, G., et al. 2010, *Sci*, **330**, 800
- Peng, C. Y., Ho, L. C., Impey, C. D., & Rix, H.-W. 2002, *AJ*, **124**, 266
- Perley, R. A., & Butler, B. J. 2013, *ApJ*, **204**, 19
- Pineda, J. L., & Bensch, F. 2007, *A&A*, **470**, 615
- Riechers, D. A., Carilli, L. C., Walter, F., et al. 2011, *ApJL*, **733**, L11
- Sharon, C. E., Baker, A. J., Harris, A. I., et al. 2015, *ApJ*, **798**, 133
- Sharon, C. E., Riechers, D. A., Hodge, J., et al. 2016, *ApJ*, **827**, 18
- Smail, I., Ivison, R. J., & Blain, A. W. 1997, *ApJL*, **490**, L5
- Su, T., Marriage, T. A., Asboth, V., et al. 2017, *MNRAS*, **464**, 968
- Swetz, D. S., Ade, P. A. R., Amiri, M., et al. 2011, *ApJS*, **194**, 41
- Tagore, A. S., & Jackson, N. 2016, *MNRAS*, **457**, 3066
- Tagore, A. S., & Keeton, C. R. 2014, *MNRAS*, **445**, 694
- Tripp, S., Neri, R., Krips, M., et al. 2012, *A&A*, **540**, A74
- Turner, J. L., Hurt, R. L., & Hudson, D. Y. 1993, *ApJL*, **413**, L19
- Vieira, J. D., Crawford, T. M., Switzer, E. R., et al. 2010, *ApJ*, **719**, 763
- Wardlow, J. L., Cooray, A., De Bernardis, F., et al. 2013, *ApJ*, **762**, 59
- Young, J. S., & Scoville, N. Z. 1984, *ApJ*, **287**, 153